# Symmetry of loop extrusion by dimeric SMC complexes is DNA-tension-dependent

Biswajit Pradhan[1], Adrian Pinto[†2], Takaharu Kanno[†3,8], Damla Tetiker[1], Martin D. Baaske[1], Erin Cutt[4], Constantinos Chatzicharlampous[5], Herwig Schüler[5], Amar Deep[6], Kevin D. Corbett[6,9], Luis Aragon[7], Peter Virnau[2], Camilla Björkegren[3,8], Eugene Kim*[1]

[1] Max Planck Institute of Biophysics, 60438 Frankfurt am Main, Germany

[2] Institut für Physik, Staudingerweg 9, Johannes Gutenberg-Universität Mainz, 55128 Mainz, Germany

[3] Karolinska Institutet, Department of Cell and Molecular Biology; Biomedicum, Tomtebodavägen 16, 171 77, Stockholm, Sweden

[4] School of Biosciences, The University of Sheffield, Sheffield, S10 2TN

[5] Center for Molecular Protein Science, Department of Chemistry, Lund University, 22100 Lund, Sweden

[6] Department of Cellular and Molecular Medicine, University of California San Diego, La Jolla CA 92093 USA

[7] DNA Motors Group, MRC Laboratory of Medical Sciences (LMS), Du Cane Road,14 London W12 0HS, UK

[8] Institute for Quantitative Biosciences, The University of Tokyo, 1-1-1 Yayoi, Bunkyo-ku, Tokyo 113-0032, Japan

[9]Department of Molecular Biology, University of California San Diego, La Jolla CA 92093 USA

[†]These authors contributed equally.

[*]Corresponding author, E-mail: eugene.kim@biophys.mpg.de

**Abstract**

Structural maintenance of chromosome (SMC) complexes organize and regulate genomes via DNA loop extrusion. During this process, the complexes increase the loop size by reeling in DNA from one or both sides of the loop. The factors governing this symmetry remain unclear. Here, we combine single-molecule analysis and molecular dynamic simulations to investigate the symmetry of loop extrusion of various SMC complexes. We find that whereas monomeric condensin and cohesin are one-sided extruders, the symmetry of dimeric SMCs, such as Smc5/6 and Wadjet, is DNA tension dependent. At low DNA tension (< 0.1pN), Smc5/6 and Wadjet extrude DNA from both sides of the loop. At higher tension, however, they transition to a behavior akin to one-sided extruders, yet still capable of extruding from one or the other side thereby switching the direction of extrusion. Our simulations further reveal that thermal fluctuations significantly influence loop extrusion symmetry, causing variations in DNA reeling rates between the two motors in the dimeric complexes and their direction switching at stalling tensions. Our findings challenge the previous view of loop extrusion symmetry as a fixed characteristic, revealing its dynamic nature and regulation by both intrinsic protein properties and extrinsic factors.

**Introduction**

Structural Maintenance of Chromosomes (SMC) complexes (here referred to as SMCs), including condensin, cohesin and the Smc5/6 complex (Smc5/6), play a critical role in organizing and maintaining

genomes across all domains of life. At the molecular level, these complexes fold DNA into loops via extrusion. The loop extrusion process has been directly observed through *in vitro* single-molecule imaging for all eukaryotic SMC complexes (*1*–*7*) and for the prokaryotic SMC Wadjet (*8*). These experiments allow us to monitor the entire kinetics of loop extrusion, from the formation and enlargement of a loop until its disruption, thus revealing important mechanistic details. One particularly intriguing and debated aspect of the mechanism is the symmetry of loop extrusion, which refers to how SMCs reel DNA into a loop at any given time. Loop extrusion can be *two-sided* (symmetrical), where SMCs reel in DNA from both sides of a loop simultaneously, or *one-sided* (asymmetrical), where DNA is primarily reeled in from one side. One-sided extrusion can become bidirectional over time by periodically switching extrusion direction (*bidirectional one-sided* loop extrusion).

So far, the symmetry of loop extrusion has been shown to vary significantly across different complexes, different species and even within the same complex under different conditions. For instance, yeast condensin has been observed to be a strictly monomeric extruder and performs one-sided extrusion (*1*), whereas human condensin exhibits a mix of one-sided and two-sided extrusion (*4*). Similarly, while initial studies suggested two-sided extrusion by cohesin (*3*), recent work indicates bidirectional one-sided extrusion by single cohesin complexes (*9*). The symmetry of loop extrusion by Smc5/6 has also been a subject of debate, with conflicting reports of two-sided (*6*) and one-sided extrusion (*9*). The factors influencing these variations remain poorly understood.

In this study, we aim to resolve these discrepancies and provide a comprehensive understanding of the symmetry of loop extrusion. To this end, we combine *in vitro* single-molecule experiments and molecular dynamics simulations to analyze the symmetry of loop extrusion for eukaryotic SMCs and the prokaryotic Wadjet complex. Our findings confirm that while monomeric condensin and cohesin performs one-sided extrusion, dimeric Smc5/6 and Wadjet complexes perform two-sided extrusion. Unexpectedly, however, we find that the observed symmetry for dimeric SMCs is strongly dependent on DNA tension. At tension above 0.1 pN, Smc5/6 and Wadjet exhibit behavior of one-sided extruders, with varying degrees of DNA slippage from the non-extruding side. Upon reaching tension near the stalling forces of loop extrusion, dimeric SMCs further transition to one-sided bidirectional extruders. In contrast, condensin and cohesin remain strictly one-sided, independent of DNA tension, with cohesin exhibiting direction switching near stalling tensions. The findings of DNA tension-dependent symmetry transition for dimeric SMCs and their direction switching at stalling tensions are corroborated by our molecular dynamic simulations. These simulations also revealed thermal fluctuation as a factor driving the heterogenous extrusion rates of the two motors in a dimeric complex and spontaneous direction switching. Overall, our findings challenge the prevailing view that SMC complexes have fixed properties, such as strictly one-sided (asymmetric) extrusion. Instead, our results suggest that loop extrusion symmetry is a dynamic process modulated by a combination of factors, including SMC dimerization, thermal fluctuations, and DNA tension.

**Results**

To assess the symmetry of DNA loop extrusion by SMC complexes,, we employed *in vitro* single-molecule fluorescence imaging and monitored loop extrusion events mediated by SMC complexes. In this assay, both ends of a DNA molecule are anchored to a passivated glass surface and stained with Sytox Orange, an intercalating dye (Fig. 1a). The DNA molecules are stretched via buffer flow to approximately 30% of their contour length. Upon introducing SMC complexes and ATP, a loop appears as a bright spot along the DNA and gradually expands, as depicted in the example kymograph of fluorescence intensities in Fig. 1b. From these kymographs, we estimate the change in DNA length within the loop and outside the loop (regions I and II) over time, based on their respective fluorescence intensities (Fig. 1c). By analyzing the slopes of these DNA length traces using linear fitting over 5-second intervals with a running time window,

we further determine the rates of DNA length change (Fig. 1d; Methods). The changes in DNA length (Fig. 1c) and their rates (Fig. 1d) reveal distinct phases of loop extrusion: an initial growth phase, where the loop forms and expands until reaching a plateau ($Rate_{loop} \approx 0$ kbp/s), followed by a mature phase characterized by transitions between loop shrinkage ($Rate_{loop} < 0$ kbp/s) and regrowth ($Rate_{loop} > 0$ kbp/s), which can occur repeatedly.

After classifying individual loop extrusion events into distinct phases (initial growth, mature growth and shrinkage), we assess the symmetry of loop extrusion during the respective phases. This is determined by comparing the rates of DNA length changes on both sides (I, II) outside the loop ($Rate_I$ and $Rate_{II}$; Fig. 1d) using a quadrant plot (Q1 to Q4; Fig. 1e). We also analyze their "ratio-of-rates" (Fig. 1e,f), which is defined as $Rate_{small}/Rate_{large}$, where $Rate_{small}$ ($Rate_{large}$) is the rate with the smaller (larger) absolute value. For two-sided extrusion, DNA strands from both I and II decrease ($Rate_{I,II} < 0$; Q3) and thus the ratios-of-rates are larger than zero (green). One-sided extrusion, where only one of the two DNA strands (I or II) decreases in length ($Rate_{Larg} < 0$), can be further divided depending on the absence ($Rate_{Small} \approx 0$, ratio-of-rates ≈ 0; red) or the presence ($Rate_{Small} > 0$, ratio-of-rates < 0; blue) of DNA slippage of the non-extruding side. The symmetry during loop shrinkage is determined similarly but with opposite signs, see Fig. S1. Instances of loop stalling, namely when both $Rate_I$ and $Rate_{II}$ are near zero (within experimental error of 0.1 kbp/s) and loop diffusion, i.e. when $Rate_{loop}$ is near zero, were excluded from further analysis. In brief, positive ratio-of-rates with data points occupying Q3 of the quadrant plot indicates two-sided extrusion; otherwise, one-sided extrusion is implied.

We first assessed the symmetry of loop extrusion by Smc5/6 and Wadjet complexes during the initial growth, mature growth and shrinkage phases (Fig. 2a-j). In the initial growth phase, Smc5/6 and Wadjet predominantly exhibit negative rates with the majority of rates falling in Q3 (Fig. 2a,h) and thus the ratio-of-rates larger than zero (Fig. 2b,i), indicating two-sided extrusion. However, during mature phase extrusion and shrinkage, we observed that Smc5/6 and Wadjet exhibit the shift of distribution of rates towards zero and positive values falling into Q2 and Q4 (Fig. 2c,e, Fig.S2a,b), leading to zero and negative values of ratios-of-rates (Fig. 2d,f,i, Fig. S2c,d). This suggests a transition from two-sided to one-sided extrusion accompanied by loop slippage, resulting in additional loop growth or shrinkage depending on the relative rates between the two processes. Notably, Wadjet showed less DNA slippage than Smc5/6 in the mature phase, evidenced by a smaller proportion of negative ratios-of-rates (Fig. 2i). Further quantification of the proportion of one-sided (with and without loop slippage) versus two-sided extrusion in each phase (Fig. 2g; Methods) confirms that two-sided extrusion by Smc5/6 and Wadjet is most prominent in the initial growth phase (52% for Smc5/6, 65% for Wadjet), while mature loop shrinkage and regrowth occur primarily through one-sided extrusion with loop slippage. Notably, this transition from two-sided to one-sided extrusion also occurs during the initial growth phase (Fig. S3a), leading to a gradual decrease of the two-sided fraction from 65% to 34% over time (Fig. S3b).

Next, we evaluated the symmetry of loop extrusion by budding yeast condensin and human cohesin (Fig. 2k-p). In contrast to Smc5/6 and Wadjet, both condensin and cohesin predominantly exhibit one-sided extrusion throughout all phases, as evidenced by the negligible fraction in Q3 (Fig. 2k,n, Fig. S2e,f,i,j) and the ratio-of-rates distributions less than zero (Fig.2l,o). Further categorization in all phases (Fig. 2m,p) confirms that both condensin and cohesin primarily perform one-sided extrusion accompanied by DNA slippage. Taken together, two-sided extrusion by Wadjet and Smc5/6 is most prominent during the initial growth phase, while in the mature phase one-sided extrusion becomes a shared feature among all SMC complexes.

Our loop extrusion traces were typically acquired with time resolutions of 100-200 ms, which could possibly miss asynchronous one-sided extrusion occurring at faster time scale during the initial growth

phase. Therefore, we repeated symmetry analysis of loop extrusion by Smc5/6 at a higher resolution of 10 ms (Fig. S3c-j) to ensure the confidence of our symmetry evaluation. The results at higher time resolution mirrored our analysis at lower resolution: Smc5/6 predominantly performs two-sided extrusion during the initial growth phase (63%; Fig. S3c-e, S3j), while mature loop shrinkage and regrowth occur mostly in a one-sided manner with slippage (Fig. S3d-g, Fig. S3j). Overall, these findings confirm that 100 or 200 ms time resolution is sufficient to determine loop extrusion symmetry .

To gain deeper insights into the experimentally observed behaviors of loop extrusion symmetry, we performed coarse-grained molecular dynamics simulations (Fig. 3). To this end, we employed a two-ring "handcuff" model for SMCs (*10*) and a bead-spring model for DNA (Fig. 3a) (*11*). In this model, the rings act as openings through which the DNA polymer is extruded with equal forces. This provides a minimalistic representation of dimeric motors. The setup resulted in non-linear loop growth with loop size plateauing at a stalling force (Fig. 3b,c), together with simultaneous decrease of DNA lengths from both sides (I,II), thus closely following our experimental observations for Smc5/6 and Wadjet (Fig. 1c). Interestingly, we observed that although the forces of the two handcuffs were equal (the values calibrated to match the stalling forces of SMCs; Fig.S4a-c; Methods), the resulting DNA reeling rates between the two motors (I,II) varied significantly (Fig. 3c, Fig. S4e,f). Overall, the simulated kymograph (Fig. S4d), time traces of the changes in DNA lengths (Fig. 3c) and their corresponding rates (Fig. S4e,f) closely resemble the typical loop extrusion patterns observed experimentally for Smc5/6 and Wadjet.

To simulate a monomeric motor, we modified hand-cuff model by eliminating force from one of the two rings (Fig. S4g,h). In most of the simulations, this resulted in the motor translocating along the DNA without carrying a loop (Fig. 3d, Fig.S4g). This is consistent with our previous observations for Smc5/6, where single complexes predominantly translocate along DNA (*6*, *12*), instead of looping. The minor fraction of looping events formed only small and transient loops which can be attributed to thermal fluctuations (Fig.S4h,k-m). Introducing a small force on the second ring of the handcuff, representing potential anchoring effects of Ycg1/Brn1 for yeast condensin (*13*, *14*) or STAG for human cohesin (*9*), prevented loop slippage of a translocating motor and thus restored loop extrusion behavior (Fig. 3d, Fig. S4i,j). For cohesin, we also incorporated a direction-switching mechanism, potentially induced by NIPBL binding (*9*), using experimentally derived switching times (Fig. 5c; Methods) in order to evaluate the symmetry behavior of a hypothetical one-sided extrusion capable of direction switching.

Next, using these models representing different SMCs we evaluated symmetry of loop extrusion (Fig. 3e-q, Fig. S4n-u). The dimeric handcuff model closely followed the behaviors of Smc5/6 and Wadjet, with most rates ($Rate_I$, $Rate_{II}$) falling in Q3 and the ratio-of-rates well above zero during initial growth (Fig. 3e-f), and differed markedly from the experimental values obtained with condensin and cohesin (Fig. 2k, n, m, p). Furthermore, our simulation consistently showed wide-spread distribution between $Rate_I$ and $Rate_{II}$, despite the two motors being identical, suggesting the influence of thermal fluctuations on the observed heterogeneity and the resulting loop extrusion symmetry. In the case of mature phases, our dimer simulation also agreed with the experimentally observed behaviors of Wadjet and Smc5/6, predominantly showing one-sided extrusion with slippage (Fig. 3g-k). The monomeric model containing anchor displayed quadrant plots and symmetric fractions (Fig. 3l-n) similar to condensin and cohesin in the initial loop growth (Fig. 2k, n, m, p). Notably, the addition of direction switching did not significantly alter the symmetry of the monomeric model in the initial growth phase, while it led to an increase in the fraction of one-sided extrusion with slippage in the mature phase (Fig. 3o-q).

Both our experiments and simulations of dimeric motors revealed a dynamic shift in loop extrusion symmetry from two-sided to one-sided extrusion behavior as the extrusion matures (Fig. 2g, j and Fig. 3k).

This mature phase appears because, under our experimental scheme with fixed end-to-end DNA, a growing loop increases the tension outside the loop, which in turn slows down the loop growth, see e.g. Fig. S3a (*1*). Indeed, the quantifications of the ratios-of-rates at different DNA tensions, extracted using the known force-extension relation for DNA (*15*) (Fig. 4a-d), revealed a steep dependency of symmetry on DNA tension for Smc5/6 (Fig. 4a) and Wadjet (Fig. 4c). Their ratio-of-rates sharply decreased from near unity to zero for Wadjet, and to negative values for Smc5/6, when the transitions from two-sided to one-sided occurred at tensions of ~0.1 pN. This shift in symmetry concomitantly occurred with a sharp decrease in loop growth rate (Fig. 4a-d), strongly suggesting the observed transition at the mature phase (Fig. 2), characterized by slow loop growth, is driven by increased DNA tension. On the other hand, both condensin (Fig. 4e,f) and cohesin (Fig. 4g,h) demonstrate consistently negative values of the ratio-of-rates as tension increases, suggesting that one-sided extrusion independent of DNA tension. The analysis of ratio-of-rates at different loop extrusion rates (Fig. 4b,d,f,h) revealed further details of the evolution of loop extrusion symmetry. In all cases, we observed that the ratios of rates sharply decrease to minimum values when the rates are close to zero, indicating that loop slippage is most pronounced when extrusion is near stalling. The observed slippage was most pronounced for Smc5/6 and cohesin (with minimum ratio of rates < - 0.5), while Wadjet exhibit the least slippage. Simulations further confirmed this strict tension-dependent symmetry transition for dimeric motors transitioning to one-sided extrusion at ~0.1 pN (Fig. 4i,j) and tension-independent one-sided extrusion for monomeric motors (Fig. 4k-n). The simulations (Fig. 4j-n) were also in agreement with highest slippage occurring near loop stalling.

Next, we questioned whether the tension-dependent symmetry transition observed for dimeric SMCs implies a complete loss of two-sided extrusion capability at higher tensions. Interestingly, our data revealed that these complexes do not entirely lose this ability, but instead extrude primarily from one side at a given time, but can switch and reel in DNA from the other side during the course of extrusion (Fig. 5a). This direction switching can be directly observed by change of $Rate_{I}$ and $Rate_{II}$ from negative to positive signs and vice versa(Fig. 5b, Fig. S5; Methods). We find that Smc5/6, on average, switches its extrusion direction once every ~27 seconds (Fig. 5c), while Wadjet switches less frequently, i.e. once every ~80 seconds (Fig. 5c, Fig. S5c). Notably, condensin switches seldomly (once every 278 s; Fig. 5c, Fig. S5b), while cohesin switches most frequently with an average interval of 18 seconds (Fig. 5c, Fig. S5a). Importantly, we find that the DNA tensions at which the first direction switching occurs are near the stalling forces of the respective complexes (Fig. 5d, Fig. S4a-c). In the case of cohesin, however, we note that the observed stalling tension is comparably lower (~0.09pN) to that of Smc5/6 and Wadjet (~0.2pN; Fig. 5d) and is close to the lower limits of our experimentally achievable force regimes, making it difficult to confirm whether the observed switching is strictly DNA-tension-dependent.

To gain deeper understanding of the mechanism underlying the direction switching of dimeric SMCs, we analyzed the simulated traces for dimeric motors where no specific switching mechanism was implemented (Fig. 5e-g). Interestingly, we observed spontaneous direction switching also occurs in simulations (Fig. 5e-f) when the DNA tension reaches characteristic stalling forces of extrusion (Fig. 5g), which is often accompanied by slippage from one side. This suggests that the observed switching by dimeric SMCs may not require any active regulatory mechanism and instead could be solely thermally driven. Furthermore, our findings demonstrate that although dimeric SMCs transition to predominantly one-sided extruders at higher tensions, they still retain the capability for bidirectional extrusion through direction changes.

Next, to minimize the impact of DNA tension on loop extrusion symmetry assessment, we monitored SMC-mediated loop extrusion on single-tethered DNA, where one end is attached to a surface while the other remains free (Fig. 6). This configuration minimizes tension changes during extrusion, primarily influenced by a mild buffer flow used for visualization. Upon addition of SMCs and ATP under constant buffer flow

(3-5 µl/min, equivalent to ~0.05-0.07 pN tension), we observed that Smc5/6 (Fig. 6a) and Wadjet (Fig. 6b) form loops with simultaneous DNA length decrease from both sides, thus indicating two-sided extrusion. Conversely, condensin at low concentrations (to prevent z-loop formation by multiple complexes which can lead to two-sided extrusion (*16*)) extruded loops with decrease of DNA length from only one side, either from the tethered side (Fig. 6c) or from the free-end side (Fig. 6d), demonstrating one-sided extrusion. Similarly, cohesin extruded loops from one-side only (Fig. 6e). Notably, we did not observe any mature loop shrinkage or regrowth, thus again supporting that the previously observed mature phase is DNA tension-driven. Instead, extrusion ceased when loops reached the DNA end, followed by either loop disruption or stalling. Under these conditions, Smc5/6 and Wadjet exhibited near 100% two-sided extrusion, while condensin and cohesin consistently displayed 100% one-sided extrusion (Fig. 6f).

Our model of two-sided loop extrusion by dimeric Smc5/6 and Wadjet complexes proposes two physically linked motors, each capable of independent DNA translocation (Fig. 7a). This is supported by our previous findings showing single Smc5/6 complexes translocating along DNA in the presence of Nse5/6 (*6*), and also by our simulations of single motor predominantly leading to translocation (Fig. 3d). To investigate the relation between translocation and extrusion further, we analyzed the speeds of translocation events for single Smc5/6 complexes at different DNA extensions (Fig. 7b,c). This revealed that translocation, like loop extrusion, speed is DNA tension-dependent, suggesting a close relationship between these two activities. Notably, however, even at the same DNA tensions, individual translocation speeds vary significantly (Fig. 7b,c), mirroring the variability in DNA reeling rates ($Rate_I$ vs $Rate_{II}$) observed for dimeric Smc5/6 during loop extrusion (Fig. 2a). This variation occurs not only between different complexes but also within a single translocation event over time (Fig. 7d-f), similar to the heterogeneous extrusion rates observed within a single loop extrusion event (e.g. Fig. 1d). Modeling of two-sided loop extrusion with two randomly chosen translocation rates at the same DNA extension yielded broad distributions of DNA reeling rates (Fig. 7g), consistent with our experimental observations. Interestingly, simulations of a modified "single handcuff" model, which exhibited predominantly translocation (Fig. 3c), also yielded highly heterogenous translocation rates (Fig. 7h,i). Collectively, these results strongly corroborate the model of two-sided loop extrusion by dimeric motors, each independently capable of DNA translocation.

**Discussion**

In this study, we provide a detailed analysis of DNA loop extrusion symmetry by various SMC complexes, unequivocally showing two-sided extrusion for dimeric complexes and one-sided extrusion for monomeric complexes. Surprisingly, we found that loop extrusion symmetry by dimeric SMCs is highly dependent on DNA tension. At low tension, dimeric motors initiate two-sided extrusion, forming a nascent loop. As the loop grows, the elevated tension in the non-extruded part of DNA opposes the ongoing extrusion. This concurrently induces slippage from one of the two motors, while the other continues extruding. This one-sided extrusion becomes dominant at ~0.1 pN tension. Further increase of DNA tension ultimately stalls loop growth at ~0.2 pN. The loop stalling is then followed by spontaneous slippage from one motor and simultaneous extrusion from the other, resulting in switching of the extrusion direction (Fig. 7j).

Our data show that Wadjet, compared to Smc5/6, shows more dominant two-sided extrusion during initial loop growth, less DNA slippage in the mature phase, and less frequent direction switching. This suggests that Wadjet is more stably associated with DNA as compared to Smc5/6. However, when the DNA tension is kept minimal throughout extrusion (via single-tethered DNA), which prevents a growing loop from slipping, stalling and direction switching, both Smc5/6 and Wadjet perform two-sided extrusion with nearly 100% efficiency.

In contrast to the dimeric SMCs, cohesin and condensin consistently exhibit one-sided extrusion throughout both initial and mature phases, regardless of varying DNA tensions. This result seemingly support the notion that these complexes function as monomeric loop extruders (*9*, *15*). However, cohesin displays frequent switching of extrusion direction when DNA tension approaches its stalling force. While this switching could be actively regulated by NIPBL subunit (*9*), it might also stem from the spontaneous switching of cohesin complexes that partially exist as dimer, as observed in other *in vivo* (*20*) *in vitro* (*3*) studies.

Our findings on Smc5/6 loop extrusion symmetry largely differ from the results of the recent preprint publication (*9*). We observed two-sided extrusion by dimeric Smc5/6, contrary to their conclusions. We attribute these discrepancies to several factors, which we elaborated in the Supplementary Text. Furthermore, throughout this study, we identified two additional factors that can influence the evaluation of loop extrusion symmetry, which are specific to *in vitro* conditions:

(1) Protein Tagging

Single-molecule analysis of SMC proteins often involves tagging and labeling for visualization on DNA. However, the impact of tagging (and labeling) on loop extrusion kinetics and symmetry is unknown. Therefore, we compared the loop extrusion symmetry for yeast-expressed Smc5/6 with Nse2- or Nse4-SNAP-tags and for E. coli expressed Nse2-HALO-tags to their respective unlabeled wild-type counterparts (Fig. S6). We observed clear differences in loop extrusion dynamics between wild-type and tagged proteins, evident in their kymographs (Fig. S6a-d). Tagged proteins formed more dynamic loops with greater movement along DNA compared to the relatively static loops formed by wild-type proteins. Mean squared displacement (MSD) analysis confirmed this, with tagged Smc5/6 loops moving 3-4 times faster than wild-type loops (Fig. S6e-h). This increased loop movement in tagged proteins stems from their higher slippage tendency. The ratio of rates for tagged proteins (Fig. S6i-k) showed skewed distributions towards -1 in all extrusion phases, indicating slippage-dominant, one-sided extrusion (Fig. S6l,m,n).

(2) Application of 'side-flow' for real-time visualization of loop extrusion

Real-time visualization of loop extrusion by SMC complexes has been typically conducted in an experimental setting, where a constant buffer flow was applied to a double-tethered DNA molecule at a large angle (~$90^0$) with respect to the double-tethered DNA (Fig. S7a). To understand how the drag force exerted by buffer flow impacts loop extrusion symmetry, we simulated a dimeric motor with a flow force applied perpendicular to the DNA axis (Fig. S7). We observed a higher proportion of two-sided extrusion in the presence of flow, evidenced by increased population in Q3 and higher ratio-of-rates. $Rate_I$ and $Rate_{II}$ became more identical as flow increased, seen in the population distribution along the Q3 diagonal and ratio-of-rates approaching unity (Fig. S7b-f). This enhanced symmetry may arise from the drag force aligning with the extrusion direction, which also counteracting DNA slippage from the loop. Importantly, however, while this explains the potential bias to observe more pronounced two-sided extrusion for dimeric motors, this fails to explain two-sided extrusion observed by monomeric extruders like cohesin under side-flow application (*2*, *3*).

Our results suggest that Smc5/6 and Wadjet will be more likely to create stable loops (by two-sided extrusion) in regions of low DNA tension *in vivo*. In the case of Smc5/6, these could be chromosome regions where high superhelical tension has been relaxed by a transformation from twist to plectonemic supercoils, structures known to be preferential substrates for loop by the complex (*12*). Wadjet may also be able to use this tension-dependent symmetry modes for the complex's specific cleavage of plasmids, as opposed to genomic DNA (*8*, *17–19*).

In conclusion, we have presented in-depth analysis of loop extrusion symmetry by various SMC complexes, revealing its variations and its different levels of dependence on external factors, such as tension and thermal fluctuations of DNA. We demonstrate two-sided extrusion of dimeric Smc5/6 and Wadjet at low tensions, transitioning to one-sided extrusion with direction switching at higher tensions. Condensin and cohesin remain one-sided extruders, with cohesin also exhibiting direction switching. The comprehensive overview of different SMCs using the unified analysis method presented here will provide the basis for future mechanistic studies of SMCs and shed light on their diverse roles in genome biology.

**Acknowledgments**: We thank Gabriel Maul for the production of biotinylating λ-DNA. AP and PV acknowledge fruitful discussions on simulations with Apratim Chatterji.

**Funding:** This work was supported by Max Planck Society (EK), European Research Council Starting Grant 101076914 (EK), Hessian Ministry of Science and Art MSCA Grant (BP), Swedish Cancer foundation, Swedish research council, and Centre for Innovative Medicine (CIMED) (CB), National Institutes of Health R35 GM144121 (KDC), Medical Research Council UKRI MC-A652-5PY00 (L.A., and E.E.C). EK, AP and PV are grateful to the Deutsche Forschungsgemeinschaft (DFG, German Research Foundation) for funding this research: Project number 233630050-TRR 146 and 464588647-CRC 1551. AP and PV gratefully acknowledge the computing time granted on the supercomputer MOGON II and III at Johannes Gutenberg University Mainz as part of NHR South-West.

**Author contributions:** BP, EK conceptualized and developed the investigation with the input from CB, TK. BP, EK, DT performed single molecule experiments. BP, EK, MDB, DT analyzed the experimental data. AP developed the simulation model and performed molecular dynamic simulations under the guidance of PV. TK, EC, CC, AD purified protein complexes. EK, CB, PV, LA, KDC, HS supervised the project. EK, BP wrote the original draft. All the authors reviewed and edited the manuscript.

**Competing interests:** All authors declare that they have no competing interests.

**Materials & Correspondence:** Original imaging data and protein expression constructs are available upon request.

**Data availability:** Source data files will be available before publication. Original imaging data are available upon request.

**Code availability:** The Python-based data analysis source code used for the analysis of the

imaging data will be available before publication. Simulation scripts are available upon request.

## Main Figure

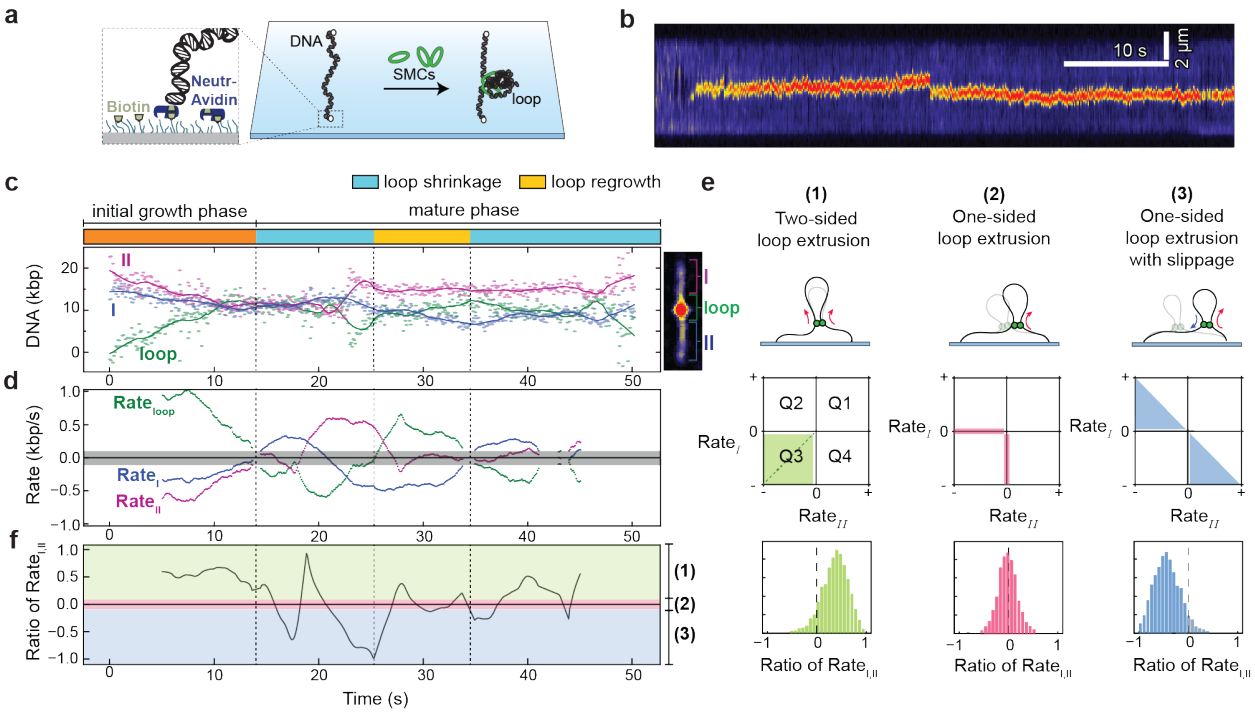


**Figure 1. Methods for evaluating loop extrusion symmetry by SMC complexes.** (a) Schematic of a flow cell containing surface-anchored lambda DNA used for monitoring DNA loop extrusion by SMCs. (b) A snapshot (left) of DNA molecule with a loop formed by Smc5/6 and the corresponding kymograph (right). (c) DNA lengths calculated from the kymograph in b for the regions outside the loop (I, II) and the loop region itself (loop), as indicated in b. (d) The rates of DNA length changes in c, extracted via linear fitting of the respective traces over 10-second intervals with a running time window. (f) The ratios of the rates, $Rate_{small}/Rate_{large}$, where $Rate_{small}$ ($Rate_{large}$) is the rate with the smaller (larger) absolute value between $Rate_I$ and $Rate_{II}$. (e) Illustration showing three different categories of symmetry (top) which can be determined by the quadrant plots of $Rate_I$ versus $Rate_{II}$ (middle) and the resulting ratio of the rates (bottom). The grid line in the quadrant plot (green) indicates the case of strictly symmetric, two-sided extrusion ($Rate_I = Rate_{II}$).

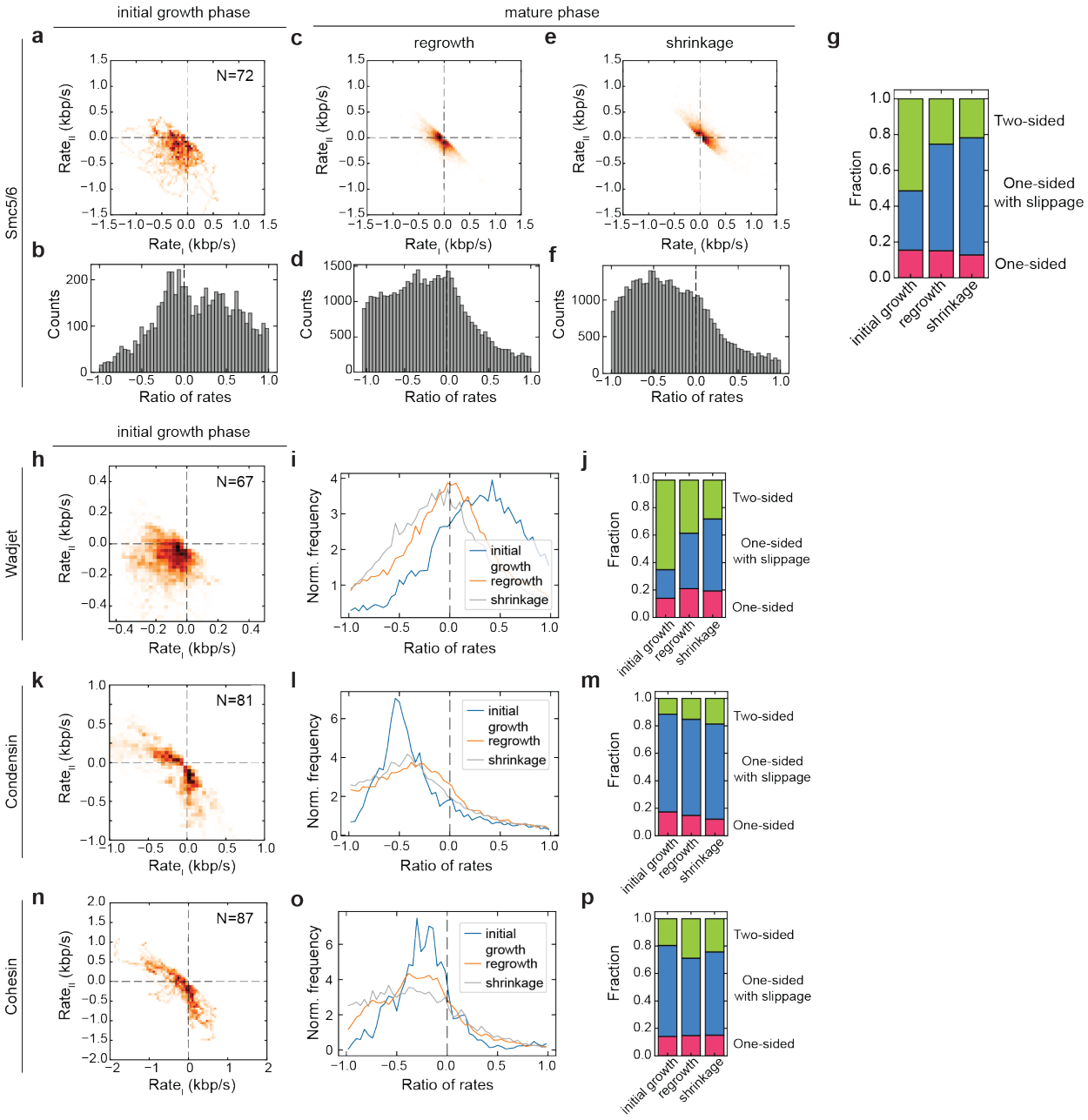


**Figure 2. Symmetry of loop extrusion by SMC complexes.** (a,c,e) Quadrant plots showing the rates outside of loop regions ($Rate_I$, $Rate_{II}$), the ratios of rates (b,d,f) and the resulting fractions (g) of different symmetries for Smc5/6 looping events during the phases of initial growth (a,b), mature regrowth (c,d) and (e,f) loop shrinkage. (h,k,n) Quadrant plots of $Rate_I$ versus $Rate_{II}$, their ratios (i,l,o) and the corresponding fractions of symmetries (j,m,p) for loop extrusion events by Wadjet (h,i,j), condensin (k,l,m) and cohesin (n,o,p) for the initial growths (h-p) and mature phases (i,j,l,m,o,p).

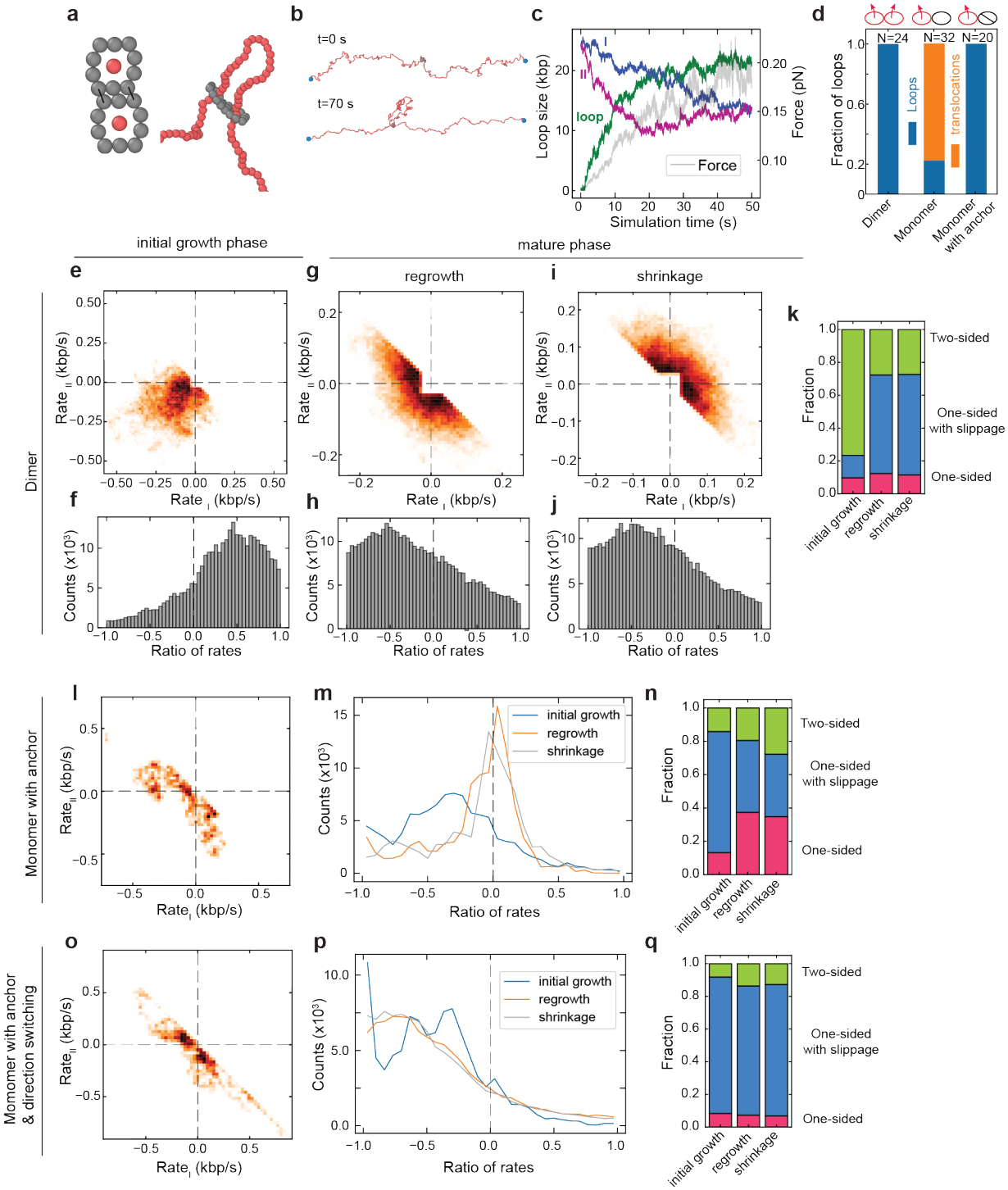


**Figure 3. Molecular dynamic simulations of dimeric and monomeric SMC-mediated loop extrusion and their symmetry evaluation.** (a) Zoomed-in images of two ring handcuff (left) and bead-spring DNA (right) model used for simulation. (b) Snapshots of a loop extrusion event at the start (top) and at the end (bottom) of the simulation run. (c) Time traces of DNA sizes for a loop extrusion simulation with two-ring handcuff model. (d) Loop extrusion probability for extrusion from both rings, single ring, and single ring in the presence of anchor. (e,g,i,l,o) Quadrant plots of RateI versus RateII, (f,h,j,m,p) the ratios of rates and

(k,n,q) the corresponding symmetry fractions for the case of dimeric motors (e-k, N=22), monomeric motor with anchor in the absence (l-n, N=20) and presence (o-q, N=12) of direction switching.

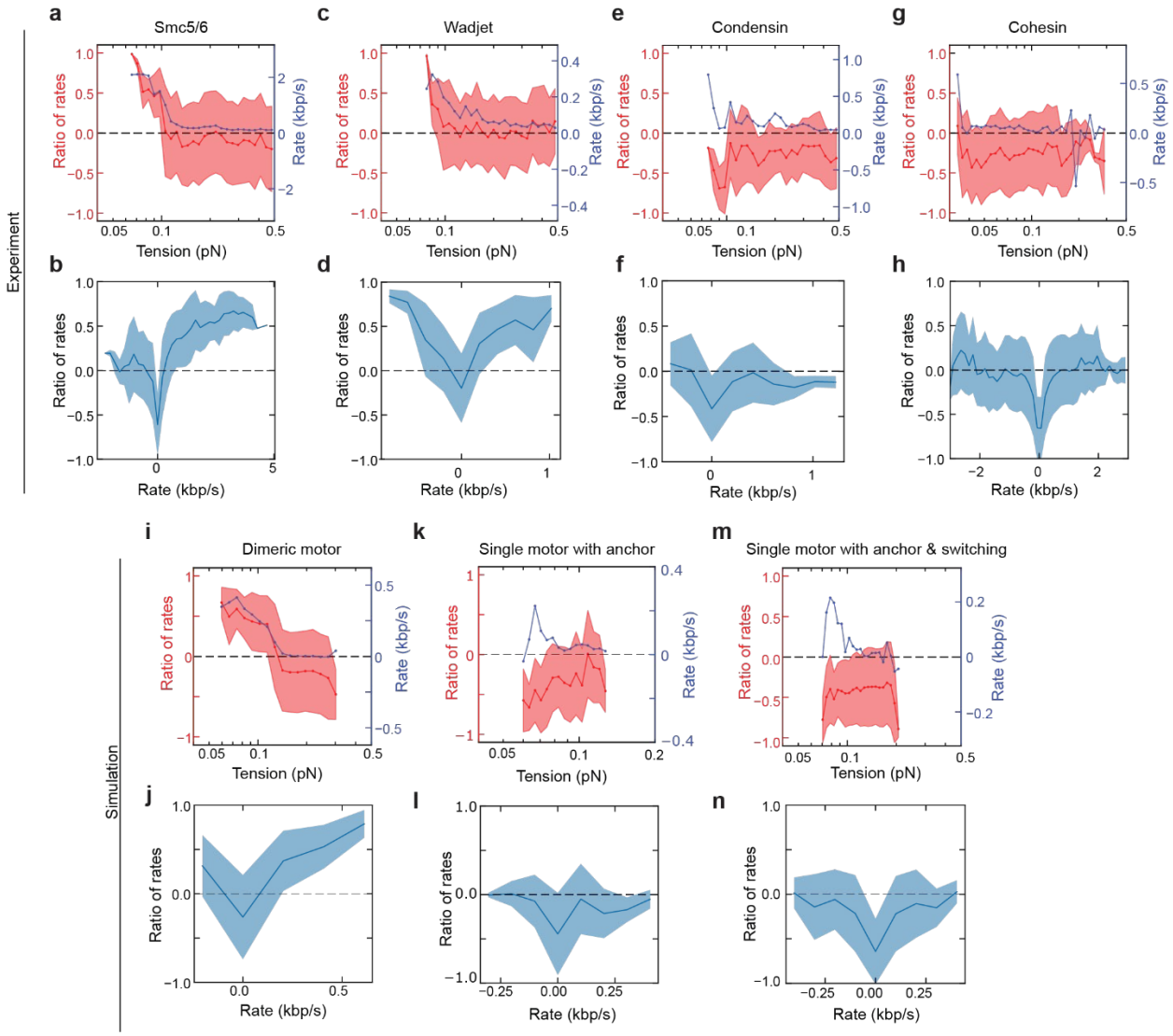


**Figure 4. Loop extrusion symmetry for dimeric SMCs is DNA tension dependent.** (a,c,e,g) Loop extrusion rates (blue) and the ratio of the rates outside the loop (red) plotted versus the tension within the DNA outside the loops for Smc5/6 (a), Wadjet (c) Condensin (e) cohesin(g). (b,d,f,h) Ratio of rates plotted against extrusion rates from the same data shown in a,c,e,g, respectively. (i,k,m) Simulated loop extrusion rates (blue) and the ratios of rates (red) at different DNA tensions for the dimeric motors and monomeric motors containing anchors without (k) and with (m) extrusion direction switching. (j,l,n) Ratio of rates plotted against extrusion rates from the same simulated data shown in i,k,m, respectively.

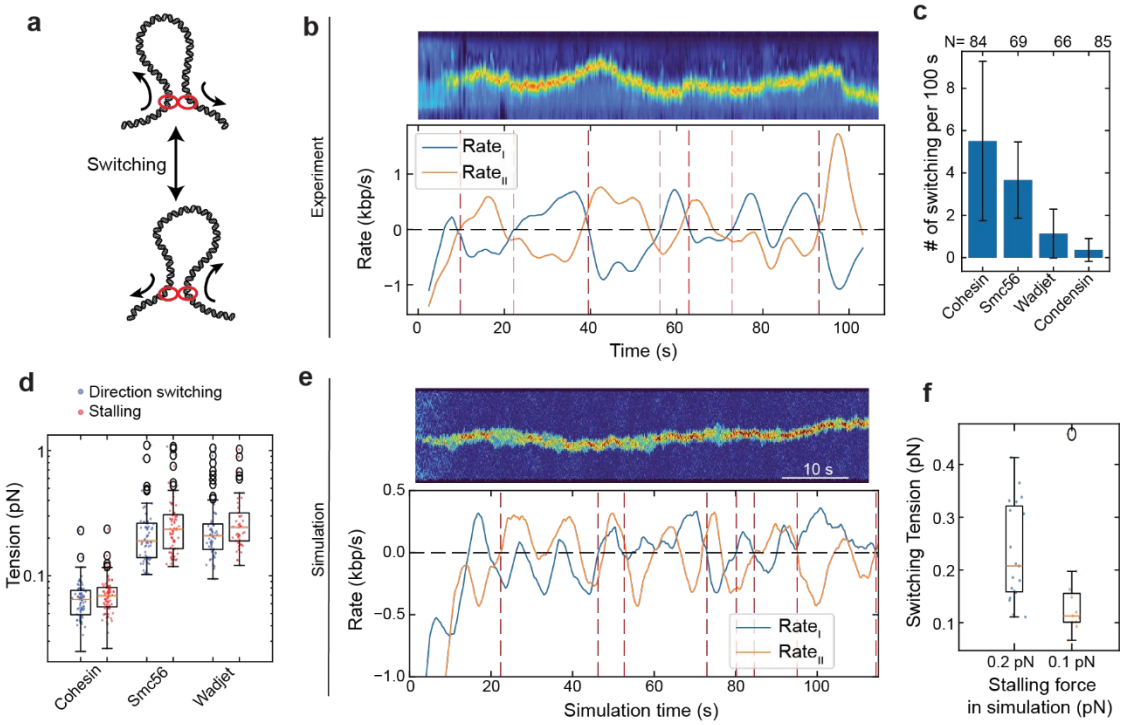


**Figure 5. Dimeric SMCs become bidirectional one-sided extruders at stalling DNA tensions.** (a) Schematic illustrating direction switching in loop extrusion by a dimeric extruder, accompanied by slippage from the non-extruding side. (b) Kymograph of Smc5/6 looping and (b) the corresponding time traces for the rates outside of loop (I,II) showing extrusion direction switching. (c) Average number of direction-switching observed for different SMC complexes. (d) Force values at which first extrusion direction switching occurred for different SMCs and their respective stalling forces. (e) Simulated kymograph and the corresponding time traces of the rates outside of the loop for dimeric motors with the vertical dashed lines indicating direction switching. (f) Force values at which the first direction switching occurred for dimers for two different stalling forces in simulations.

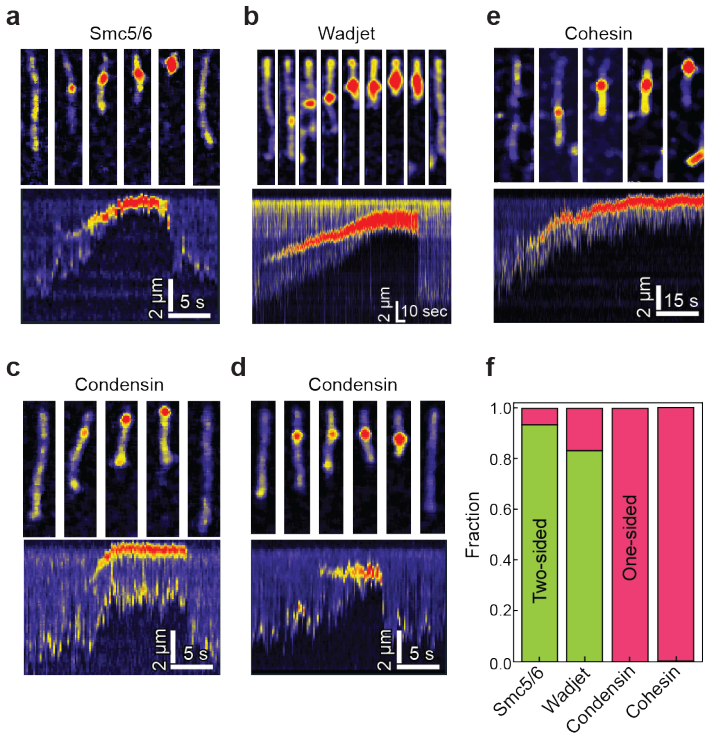


**Figure 6. Two-sided extrusion by dimeric SMC complexes on single-tethered DNA.** (a-d) Snapshots of DNA molecules (top) and the corresponding kymographs (bottom), showing loop extrusion events on single-tethered DNA for Smc5/6 (a), Wadjet (b), condensin (c,d) and cohesin (e). (f) Fraction of symmetry estimated for different SMCS on single-tethered DNA.

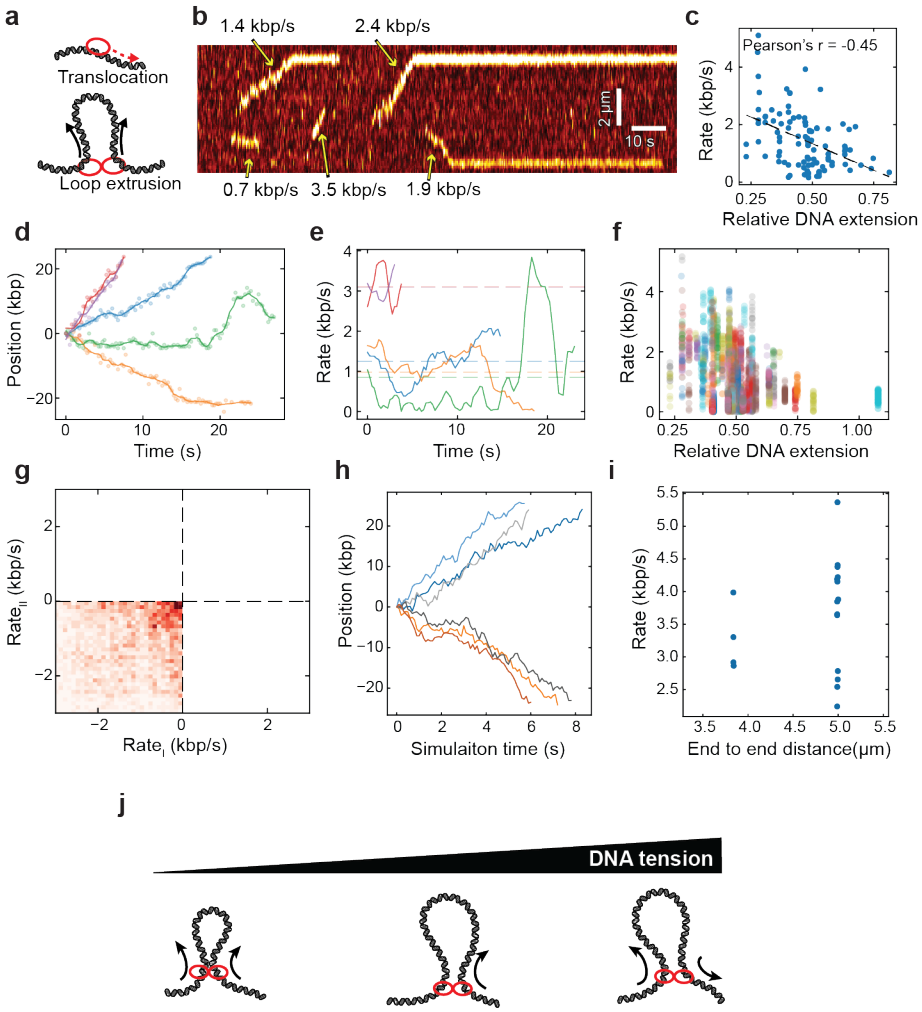


**Figure 7. Dimeric SMCs are composed of two single motors which alone can translocate along DNA.** (a) A model of dimeric SMC mediated loop extrusion and monomeric SMC mediated translocation. (b) A kymograph showing multiple translocating events from Alexa647-labeled Smc5/6 octameric complexes. (c) Translocation rates at different DNA extension values. (d) Time traces of multiple translocation events and (e) the corresponding rates extracted via linear fitting over 3 s time interval. (f) Scatter plot showing translocation rates versus relative DNA extensions with heterogenous rate distributions for a single Smc5/6 indicated by a distinct color. (g) Model quadrant plot demonstrating loop extrusion with two translocating motors, using distributions of two translocation rates from Fig. f at the same DNA extension. (h) Examples of simulated translocation traces of single handcuff motor and (h) their rate distributions. (i) Heterogeneous translocation rates in simulations as a function of grafting distance. (j) model of loop extrusion symmetry for dimeric SMCs.

## Reference

1. M. Ganji, I. A. Shaltiel, S. Bisht, E. Kim, A. Kalichava, C. H. Haering, C. Dekker, Real-time imaging of DNA loop extrusion by condensin. *Science* **360**, 102–105 (2018).

2. I. F. Davidson, B. Bauer, D. Goetz, W. Tang, G. Wutz, J.-M. Peters, DNA loop extrusion by human cohesin. *Science* **366**, 1338–1345 (2019).

3. Y. Kim, Z. Shi, H. Zhang, I. J. Finkelstein, H. Yu, Human cohesin compacts DNA by loop extrusion. *Science* **366**, 1345–1349 (2019).

4. M. Kong, E. E. Cutts, D. Pan, F. Beuron, T. Kaliyappan, C. Xue, E. P. Morris, A. Musacchio, A. Vannini, E. C. Greene, Human Condensin I and II Drive Extensive ATP-Dependent Compaction of Nucleosome-Bound DNA. *Molecular Cell* **79**, 99-114.e9 (2020).

5. T. L. Higashi, G. Pobegalov, M. Tang, M. I. Molodtsov, F. Uhlmann, A Brownian ratchet model for DNA loop extrusion by the cohesin complex. *eLife* **10**, e67530 (2021).

6. B. Pradhan, T. Kanno, M. Umeda Igarashi, M. S. Loke, M. D. Baaske, J. S. K. Wong, K. Jeppsson, C. Björkegren, E. Kim, The Smc5/6 complex is a DNA loop-extruding motor. *Nature* **616**, 843–848 (2023).

7. S. Golfier, T. Quail, H. Kimura, J. Brugués, Cohesin and condensin extrude DNA loops in a cell cycle-dependent manner. *eLife* **9**, e53885 (2020).

8. B. Pradhan, A. Deep, J. König, M. D. Baaske, K. D. Corbett, E. Kim, Loop extrusion-mediated plasmid DNA cleavage by the bacterial SMC Wadjet complex. bioRxiv [Preprint] (2024). https://doi.org/10.1101/2024.02.17.580791.

9. R. Barth, I. F. Davidson, J. van der Torre, M. Taschner, S. Gruber, J.-M. Peters, C. Dekker, SMC motor proteins extrude DNA asymmetrically and contain a direction switch. bioRxiv [Preprint] (2023). https://doi.org/10.1101/2023.12.21.572892.

10. C. A. Brackley, J. Johnson, D. Michieletto, A. N. Morozov, M. Nicodemi, P. R. Cook, D. Marenduzzo, Nonequilibrium Chromosome Looping via Molecular Slip Links. *Phys. Rev. Lett.* **119**, 138101 (2017).

11. S. Wettermann, R. Datta, P. Virnau, Influence of ionic conditions on knotting in a coarse-grained model for DNA. *Front. Chem.* **10** (2023).

12. K. Jeppsson, B. Pradhan, T. Sutani, T. Sakata, M. Umeda Igarashi, D. G. Berta, T. Kanno, R. Nakato, K. Shirahige, E. Kim, C. Björkegren, Loop-extruding Smc5/6 organizes transcription-induced positive DNA supercoils. *Molecular Cell*, doi: 10.1016/j.molcel.2024.01.005 (2024).

13. M. Kschonsak, F. Merkel, S. Bisht, J. Metz, V. Rybin, M. Hassler, C. H. Haering, Structural Basis for a Safety-Belt Mechanism That Anchors Condensin to Chromosomes. *Cell* **171**, 588-600.e24 (2017).

14. I. A. Shaltiel, S. Datta, L. Lecomte, M. Hassler, M. Kschonsak, S. Bravo, C. Stober, J. Ormanns, S. Eustermann, C. H. Haering, A hold-and-feed mechanism drives directional DNA loop extrusion by condensin. *Science* **376**, 1087–1094 (2022).

15. I. F. Davidson, R. Barth, M. Zaczek, J. van der Torre, W. Tang, K. Nagasaka, R. Janissen, J. Kerssemakers, G. Wutz, C. Dekker, J.-M. Peters, CTCF is a DNA-tension-dependent barrier to cohesin-mediated loop extrusion. *Nature* **616**, 822–827 (2023).

16. E. Kim, J. Kerssemakers, I. A. Shaltiel, C. H. Haering, C. Dekker, DNA-loop extruding condensin complexes can traverse one another. *Nature* **579**, 438–442 (2020).

17. A. Deep, Y. Gu, Y.-Q. Gao, K. M. Ego, M. A. Herzik, H. Zhou, K. D. Corbett, The SMC-family Wadjet complex protects bacteria from plasmid transformation by recognition and cleavage of closed-circular DNA. *Molecular Cell* **82**, 4145-4159.e7 (2022).

18. H. W. Liu, F. Roisné-Hamelin, B. Beckert, Y. Li, A. Myasnikov, S. Gruber, DNA-measuring Wadjet SMC ATPases restrict smaller circular plasmids by DNA cleavage. *Molecular Cell* **82**, 4727-4740.e6 (2022).

19. F. Roisné-Hamelin, H. W. Liu, M. Taschner, Y. Li, S. Gruber, Structural basis for plasmid restriction by SMC JET nuclease. *Molecular Cell*, doi: 10.1016/j.molcel.2024.01.009 (2024).

20. F. Ochs, C. Green, A. T. Szczurek, L. Pytowski, S. Kolesnikova, J. Brown, D. W. Gerlich, V. Buckle, L. Schermelleh, K. A. Nasmyth, Sister chromatid cohesion is mediated by individual cohesin complexes. *Science* **383**, 1122–1130 (2024).

21. E. E. Cutts, S. Saravanan, G. L. M. Fisher, D. S. Rueda, L. Aragon, Substrate accessibility regulation of human TopIIa decatenation by cohesin. bioRxiv [Preprint] (2023). https://doi.org/10.1101/2023.11.20.567865.

22. F. Weissmann, G. Petzold, R. VanderLinden, P. J. Huis in 't Veld, N. G. Brown, F. Lampert, S. Westermann, H. Stark, B. A. Schulman, J.-M. Peters, biGBac enables rapid gene assembly for the expression of large multisubunit protein complexes. *Proceedings of the National Academy of Sciences* **113**, E2564–E2569 (2016).

23. E. Kim, A. M. Gonzalez, B. Pradhan, J. van der Torre, C. Dekker, Condensin-driven loop extrusion on supercoiled DNA. *Nat Struct Mol Biol* **29**, 719–727 (2022).

24. B. Pradhan, R. Barth, E. Kim, I. F. Davidson, B. Bauer, T. van Laar, W. Yang, J.-K. Ryu, J. van der Torre, J.-M. Peters, C. Dekker, SMC complexes can traverse physical roadblocks bigger than their ring size. *Cell Reports* **41**, 111491 (2022).

25. J. F. Marko, E. D. Siggia, Stretching DNA. *Macromolecules* **28**, 8759–8770 (1995).

26. C. Plesa, D. Verschueren, S. Pud, J. van der Torre, J. W. Ruitenberg, M. J. Witteveen, M. P. Jonsson, A. Y. Grosberg, Y. Rabin, C. Dekker, Direct observation of DNA knots using a solid-state nanopore. *Nature Nanotech* **11**, 1093–1097 (2016).

27. R. Kumar Sharma, I. Agrawal, L. Dai, P. S. Doyle, S. Garaj, Complex DNA knots detected with a nanopore sensor. *Nat Commun* **10**, 4473 (2019).

28. D. Racko, F. Benedetti, D. Goundaroulis, A. Stasiak, Chromatin Loop Extrusion and Chromatin Unknotting. *Polymers* **10**, 1126 (2018).

29. Synergy of topoisomerase and structural-maintenance-of-chromosomes proteins creates a universal pathway to simplify genome topology | PNAS. https://www.pnas.org/doi/full/10.1073/pnas.1815394116.

30. A. Goloborodko, M. V. Imakaev, J. F. Marko, L. Mirny, Compaction and segregation of sister chromatids via active loop extrusion. *eLife* **5**, e14864 (2016).

31. J. A. Anderson, J. Glaser, S. C. Glotzer, HOOMD-blue: A Python package for high-performance molecular dynamics and hard particle Monte Carlo simulations. *Computational Materials Science* **173**, 109363 (2020).

## Methods

### Protein expression and purification

*The Smc5/6 complex overexpression and purification from S. cerevisiae*

*S. cerevisiae* Hexameric (Smc5, Smc6 and Nse1-4) and octameric (Smc5, Smc6 and Nse1-6) Smc5/6 complexes were purified according to the published protocol (Pradhan et al. Nature). Briefly, the Smc5/6 complex were overexpressed by galactose-inducible system in YEP-lactate medium and isolated with tandem affinity purification system using IgG Sepharose 6 FF (VWR, 17-0969-01) and calmodulin Sepharose 4B (Merck, GE17-0529-01). The eluate was concentrated using Vivaspin 20 100K MWCO ultrafiltration unit (Sartorius, VS2041), with simultaneous exchange to STO500 buffer (50 mM Tris-HCl pH 8.0, 500 mM NaCl, 2 mM $MgCl_2$, 0.5 mM tris(2-carboxyethyl)phosphine (TCEP), 10% glycerol, 0.1% IGEPAL CA-630). Fluorescently labelled hexameric Smc5/6 complexes that carry a C-terminal SNAP-tag on the Nse2 subunit or the Nse4 subunit were overexpressed, purified, and labelled according to the published protocol (Pradhan et al. Nature). Briefly, the eluate from IgG Sepharose 6 FF was incubated with SNAP-Surface-Alexa Flour 647 (New England Biolabs, S9136S) at 4 ºC overnight. After the reaction, the excess label was eliminated by 100K MWCO Amicon Ultra centrifugal filter (Merck, UFC5100) with concomitant buffer exchange to STO500 buffer.

*The Smc5/6 complex overexpression and purification from E.coli*

*S. cerevisiae* hexameric Smc5/6 complex (Smc5, Smc6, and Nse1-4) was also produced in *Escherichia coli* using the vectors and protocols from the Prof. S. Gruber group (Taschner et al, EMBO, 2021; Roman et al., bioRxiv 2023) with modifications. Plasmids were transformed into Rosetta 2(DE3) cells (Novagen). Liquid cultures of 2x1.5 L were prepared in Terrific Broth with antibiotics and grown in Schott flasks in a LEX bioreactor (Epiphyte3, Canada) at 37ºC until the cultures reached an optical density of approximately 2.0, measured at 600 nm. Then, the temperature was lowered to 18ºC, and protein expression was induced using 0.5 µM isopropyl ß-D-1-thiogalactopyranoside (IPTG) for 16 h. Cells were lysed by freeze-thaw cycles and sonication in lysis buffer (50 mM Tris pH 7.5, 300 mM NaCl, 5% glycerol, 2 mM TCEP, 0.01% NP40) supplemented with 2.5 kU of nuclease (Thermo Scientific, 88701) and protease inhibitor cocktail (Sigma-Aldrich, S8830). Cleared lysate was applied to a 5 ml Strep-Tactin XT 4 Flow high capacity column (IBA, 2-5028-001). After washing with 10 CV lysis buffer, bound proteins were eluted using BXT buffer (IBA, 2-1042-025). Fractions containing target protein were applied to a 5 ml HiTrap Heparin HP column (Cytiva). After washing with 5 CV low-salt HP buffer (20 mM Tris pH 7.5, 200 mM NaCl, 2 mM TCEP, 0.01% NP40), bound proteins were eluted with a 5 CV continuous gradient of 200 mM to 1 M NaCl in low-salt HP buffer. The peak fractions were concentrated using a 30 kDa MWCO Vivaspin-20 concentrator (Sartorius, VS2021) and further purified by size exclusion chromatography (SEC) using a Superdex 200 Increase 10/300 GL column (Cytiva) in SEC buffer (20 mM Tris-HCl pH 7.5, 250 mM NaCl, 1 mM TCEP and 0.05% NP40). The peak fractions were concentrated again and snap-frozen in liquid nitrogen. For purification of Smc5/6 complex with a C-terminal Halo Tag on the Nse4 subunit for fluorescent labeling, 3x StrepTrap HP 1mL columns (Cytiva) were used and proteins were eluted with lysis buffer containing 2.5 mM desthiobiotin. The SEC peak fractions were incubated with 14 µM Janelia Fluor646 HaloTag ligand (Promega, GA1120) at room temperature for 1 h and excess label was eliminated by 100K MWCO Amicon Ultra centrifugal filter with concomitant buffer exchange to STO500 buffer.

*Wadjet overexpression and purification*

The maleimide-labelable *Pseudomonas aeruginosa* PA14 JetABC complex was purified as previously described (*8*). Briefly, the $His_6$-JetA + untagged JetB coexpression construct (*17*) was modified to remove native cysteine residues in JetA (C36A, C355A) and to insert a cysteine into a disordered loop region of JetA (C66; this residue was added between JetA residues A65 and S66 in the wild-type sequence). For JetC expression, a tagless JetC construct was used, as tagless JetC efficiently binds to $Ni^{2+}$ affinity resin (*17*).

JetAB and JetC proteins were expressed in *E. coli* Rosetta2 pLysS (EMD Millipore) by growing cells in 2XYT media at 37°C until the $OD_{600}$ reached 0.55–0.75, followed by induction with 0.33 mM IPTG. Cultures were incubated overnight (~16 hours) at 20°C for protein expression. Cells were harvested by centrifugation, and pellets were resuspended in ice-cold buffer containing 50 mM Tris pH 7.5, 300 mM NaCl, 10 mM imidazole, 10% glycerol, and 2 mM β-mercaptoethanol. The resuspended cells were lysed by sonication, and the lysate was clarified by centrifugation. Proteins were purified using $Ni^{2+}$ affinity chromatography (Ni-NTA Superflow, Qiagen). JetAB and JetC proteins were further purified by anion-exchange chromatography (HiTrap Q HP, Cytiva) using a buffer containing 20 mM Tris pH 7.5, 2 mM β-mercaptoethanol, and 50 mM to 1 M NaCl. The eluted proteins were concentrated and passed through a Superose 6 Increase 10/300 GL size exclusion column (Cytiva) in a buffer containing 20 mM HEPES pH 7.0, 150 mM KCl, and 1 mM TCEP (tris(2-carboxyethyl)phosphine).

For JetAB labeling with a maleimide-based fluorescent tag, the JetAB complex was mixed with Janelia Fluor 646 dye (Tocris) at a 1:20 molar ratio of JetAB to dye. The mixture was incubated overnight at 4°C with constant gentle rotation. The next day, excess dye was removed by passing the complex through a Superose 6 Increase 10/300 GL size exclusion column (Cytiva), and the conjugation efficiency was measured using a NanoDrop (Thermo Scientific). The average labeling efficiency was determined to be ~70% for the two labeling sites in the JetA2B4 complex.

Purified JetAB (labeled JetAB) and JetC subunit proteins were mixed in a specific stoichiometric ratio to obtain the $JetA_2B_4C_4$ complex. Any aggregated particles were removed through another round of size exclusion chromatography. The purity of the samples was assessed using SDS-PAGE analysis, and the samples were flash-frozen in liquid nitrogen and stored at -80°C until use.

*Cohesin overexpression and purification*

Human cohesin was purified as described previously (*21*). In brief, Cohesin STAG1 tetramer complex was cloned into a pBIG2ab vector (*22*) with a C-terminal 3C-His10 tag on SMC3 and a C-terminal 3C-ybbr-tev-strepII on STAG1. NIBPL with a deletion of N-terminal 1162, an N-terminal MBP and C-terminal 3C-ybbr-tev-strepII tag was cloned into a pLIB vector (*22*). All constructs were transposed into DH10EMBacY to generate bacmids, and purified bacmid transfected into SF9 cells. After 72 hours, virus was harvested and further amplified in SF9 cells before being used for expression in either SF9 for 72 hours. Cell pellets were resuspended in purification buffer (20 mM HEPES [pH 8], 300 mM KCl, 5 mM MgCl2, 1 mM DTT, 10% glycerol) supplemented with 1 Pierce protease inhibitor EDTA–free tablet (Thermo Scientific) per 50mL and 25 U/mL of Benzonase (Sigma) and lysed with a dounce homogeniser followed by brief sonication. Lysate was cleared with centrifugation, then loaded on to a StrepTrap HP (GE), washed with purification buffer and eluted with purification buffer supplemented with 5 mM Desthiobiotin (Sigma). Protein containing fractions were pooled, diluted 2-fold with Buffer A (20 mM HEPES [pH 8], 5 mM MgCl2, 5% glycerol, 1 mM DTT), loaded on to HiTrap Heparin HP column (GE), washed with Buffer A with 250 mM NaCl, then eluted with a gradient up to 2M NaCl. StrepII tags were cleaved with Tev protease overnight prior to size exclusion chromatography with a Superose 6 increase 10/300 column in purification buffer.

*Condensin overexpression and purification*

The pentameric S. cerevisiae condensin complex was prepared according to the previously published expression and purification procotols (*1*).

**Single-molecule imaging of DNA loop extrusion by SMC complexes**

Loop extrusion assay was performed as described in Pradhan et al. (*6*) Concisely, λ-DNA (unless otherwise specified) with biotin at both terminals was anchored to glass slides functionalized with streptavidin in a flow cell channel. The DNA solution was introduced at a flow rate of 2-3 µl $min^{-1}$, resulting in an average distance of approximately 5 µm between the two ends of the DNA molecule. This structure was designated as double-tethered DNA. Single-tethered DNA was obtained by incubating λ-DNA with biotin on one end until the desired DNA density was attained.

Real-time loop extrusion was achieved by introducing SMC complexes in an imaging buffer. A constant buffer flow of 5 to 10 µL/min was maintained when employing single-tethered DNA. The typical imaging buffer consisted of 100 nM Sytox Orange, 100 mM NaCl, 7.5 mM MgCl2 in TX-buffer (100 mMTris-HCl pH 7.5, 0.5 mg $ml^{-1}$ BSA, 0.2 mMTCEP, 1 mM ATP, 30 mM d-glucose, 2 mM trolox, 10 nM catalase, 37.5 µM glucose oxidase). The specific salt concentrations, temperature, and DNA substrates for different SMC complexes are elaborated in the following section.

Typically, ten thousand images with an acquisition time of 100 ms (unless otherwise specified) were recorded and stored for subsequent analysis. For wildtype SMC complexes, solely a 561 nm laser was used to visualize the DNA. In the case of labeled SMC complexes, both 561 nm and 640 nm lasers were irradiated alternately to image both the DNA and the SMC complexes.

*Smc5/6*

0.5 to 1 nM WT Smc5/6 was utilized for loop extrusion in an imaging buffer containing 100 mM NaCl, 7.5 mM MgCl2, and 100 to 200 nM Sytox Orange at 30°C. For fluorophore-labeled Smc5/6 complexes, concentrations of 1 to 2 nM were used.

*Wadjet*

A 44 kbp DNA substrate was utilized for loop extrusion with Wadjet as previously described (*23*). A 100 pM of fluorophore-labeled JetABC in an imaging buffer containing 100 mM NaCl, 10 mM MgCl2, and 100 nM Sytox Orange was introduced to the flow cell at 30°C for loop extrusion.

*Cohesin*

In a step-wise dilution, cohesin tetramer and NIPBL were mixed at a ratio of 1:2.5 and incubated for 1 minute at room temperature before diluting to the final concentrations. For stop flow experiments, 0.5-1 nM of cohesin and 2.5 times NIPBL was used in an imaging buffer containing with 50 mM NaCl, 7.5mM MgCl2. All experiments with single tethered DNA were done with 0.5-0.75 nM of cohesin and 2.5 times NIPBL with the same buffer condition.

*Condensin*

1 nM WT condensin was introduced in an imaging buffer containing 50 mM NaCl, 2.5 mM MgCl2, and 200 to 500 nM Sytox Orange at room temperature. For single-tethered DNA experiment, 2nM protein concentration was used instead.

**Single-molecule imaging analysis for loop extrusion symmetry**

DNA molecules were visualized using TIRF microscopy and recorded as image sequences. Individual molecules were cropped and saved as TIFF image stacks. Kinetic information, including loop positions and segment intensities, was extracted using custom software ((*24*), code available at: https://github.com/biswajitSM/LEADS). Briefly, kymographs were constructed by summing pixel intensities across the DNA axis at each time point. Loop positions were identified, and intensities within a 9-pixel window around the loop peak were recorded. Intensities on both sides of the loop (I and II) were also collected. Segment intensities were converted to kilobases, assuming the total intensity represented the full DNA substrate length (48.5 kb for λ-DNA).

Segment sizes were smoothed using a Savitzky-Golay filter (scipy, cite) to calculate rates of change. Rates of loop extrusion were calculated at each time point using a 5-second ($\Delta t$) interval:

$$Rate_{loop} = \frac{Size_{loop}(t+\Delta t/2) - Size_{loop}(t-\Delta t/2)}{\Delta t}.$$

Similarly, $Rate_I$ and $Rate_{II}$ were calculated by using the sizes of segments I and II (Fig. 1d).

The ratio-of-rates was calculated as:

$$Ratio_{I,II}(t) = \frac{min(Rate_I(t), Rate_{II}(t))}{max(Rate_I(t), Rate_{II}(t))}.$$

The initial growth phase was defined as the first 20 seconds with positive $Rate_{loop}$. Subsequent loop size changes were categorized as "regrowth" ($Rate_{loop}$ > 0.05 kbps) or "shrinkage" ($Rate_{loop}$ < -0.05 kbps), collectively termed the "mature phase." Time points with $Rate_{loop}$ between -0.05 and 0.05 kbps were excluded from further analysis. Ratio-of-rates for each phase were used for symmetry estimation. ratio-of-rates > 0.1 were classified as two-sided extrusion, ratio-of-rates < -0.1 as one-sided with slippage, and ratio-of-rates between -0.1 and 0.1 as one-sided (Fig. 3).

**Stalling force estimation**

Tension on the DNA at each time point were calculated from the relative extension of the DNA outside the loop as $r = \frac{L}{L^C_{nonloop}}$, where L is the end to end length of the double tethered DNA and $L^C_{nonloop}$is the contour length of the DNA out the loop (size of segments I and II combined converted to µm).

Then the tension at each time point was calculated as $F = \frac{k_B T}{L_p}\left(r + \frac{1}{4(1-r)^2} - \frac{1}{4}\right)$ where $k_BT$=4.1 pN.nm; $L_p$ is the persistence length of the DNA (*25*). Both persistence length and DNA length per base pair were obtained from Davidson et al.(*15*), measured under the same experimental conditions used in this study.

To calculate the stalling force, we use the DNA tension when the loop reaches its maximum size. This is automatically obtained by taking the mean of the tension at loop sizes exceeding 95% of the values observed 50 seconds after loop initiation.

To obtain the relationship between tension and the ratio-of-rates, logarithmically spaced bins were created, spanning the range from the minimum to the maximum tension observed across all molecules for a specific SMC complex. Subsequently, all ratio-of-rates associated with each bin were identified, and their average and standard deviation were computed.

**Switching direction**

Direction switching events during one-sided extrusion were identified automatically. The $Rate_{I}$ and $Rate_{II}$ values were smoothed using a Savitzky-Golay filter with a window length of 51 points. Time points where either $Rate_{I}$ or $Rate_{II}$ crossed zero were initially identified as potential crossing points. To qualify as a true direction-switching point, the crossing point had to meet the following criteria: 1) The mean values of both $Rate_{I}$ and $Rate_{II}$ since the last crossing point exceeded a threshold of 0.05 kbps. 2) After the crossing point, $Rate_{I}$ and $Rate_{II}$ had opposite signs. 3) Both $Rate_{I}$ or $Rate_{II}$ had changed its sign since the last switching point. The number of switching events per molecule was normalized to 100 seconds. The mean and standard deviation of switching frequencies were then calculated across all molecules (Fig. 5c).

**Fluorescent labeling efficiency estimation for E.coli expressed Smc5/6**

The concentration of E.coli-expressed Smc5/6 labeled with JF646 was estimated using a Bradford assay with BSA as the standard. This sample was then diluted to a 1 μM stock concentration. Subsequently, the concentration of JF646 was determined through fluorescence correlation spectroscopy (FCS), using a Zeiss LSM 880 Observer Airyscan microscope. 1 nM ATTO647N was used to calibrate for the detection volume of the confocal microscope. For FCS analysis, the stock Smc5/6 sample was further diluted to 1 nM in the imaging buffer, and autocorrelation data was recorded. The resulting autocorrelation curves were fitted with both diffusion and blinking components, in the Zeiss software. This analysis resulted in a JF646 concentration of 0.65 nM, implying a 65% labeling efficiency. However, a subsequent observation was made: post-incubation of the sample in an ice bath for an hour, the labeling efficiency decreased to 40%. Thus, we establish a labeling efficiency range of 40% to 65% for the E.coli-expressed Smc5/6.

**Molecular Dynamic Simulation**

Coarse-grained simulations of DNA are based on a standard bead-spring model: Beads are connected with FENE springs and chain stiffness is implemented with a cosine-type potential with amplitude $\kappa$. Monomers interact via a repulsive Weeks-Chandler-Andersen potential which accounts for excluded volume effects. Simulation parameters (unit of length $\sigma$, numbers of beads in a chain N and stiffness $\kappa$) are matched with experiments via an approach detailed in Ref. (*11*): As charges are not modelled explicitly, we determine the effective diameter with an approach based on polyelectrolyte theory for given ionic conditions. In addition, we match persistence and contour length, which yield $\kappa$ and N respectively. This model was shown to reproduce structural and topological properties of DNA in good agreement with corresponding experiments (*26*, *27*). All parameters used in this work are given in table 1.

| | |
|---|---|
| Number of monomers | 3026 |
| Default graft distance | 5μm |
| FENE constant K | 30 |

| | |
|---|---|
| FENE constant $r_0$ | 1.5 |
| Bending $\kappa$ | 6.549 |
| WCA constant $\sigma$ | 1 |
| WCA constant $\varepsilon$ | 1 |

Table 1: Simulation parameters representing $\lambda$-DNA (48502 bp), ionic conditions equivalent to 115mM NaCl and a persistence length of 35nm.

The SMC protein complex is modeled using a simplified handcuff structure, consisting of two rings, each composed of 10 monomers as proposed in Ref. (*10*). By default, this handcuff structure is initially placed at the center of the DNA polymer chain. These rings act as openings through which the polymer is extruded or slipped during the simulation. This double loop structure (*10*, *28*) has the advantage of simpler representations such as dynamic bonds between opposing sites of DNA (*29*, *30*) that it allows for the implementation of an explicit driving force and a more detailed distinction between two-sided and one-sided extruders, which is given in units of $k_BT/\sigma$. The polymer's ends are tethered to a wall which is interacting with the polymer via a 9-3 Lennard-Jones potential. The mass of all beads is fixed to 1, while the mass of the center of mass of the handcuff is set to 2.75 (*10*). To perform extrusion, we compute the component normal to the plane of each of the rings and give an extrusion force to the monomers which are closest to the respective rings along these normal components. Corresponding equal and opposite forces are applied to the handcuff for equivalence. Using this approach, we can simulate one-sided or two-sided extrusion by varying the magnitude of force each of the ring applies.

Note that for the computation of stalling and extrusion forces in experimental units we apply the Marko-Siggia equation (see section on stalling forces), which is based on the extension of the unextruded fraction of DNA. Dimeric extruder simulations, e.g., which require a force of 0.08 $k_BT/\sigma$ correspond to a stalling force of about 0.2 pN while 0.05 $k_BT/\sigma$ correspond to a stalling force of 0.1 pN.

We apply a small force (0.013 $k_BT/\sigma$) to the second ring during one-sided extrusion to mimic anchoring of one-sided motors. The magnitude of this force is such that it cannot cause any extrusion on its own and just opposes the slipping that happens during one-sided extrusion. Further, we also implement a one-sided switching motor by periodically switching the direction of extrusion. The switching times are randomly drawn from the experimental switching time distributions.

While our coarse-grained model already provides a mapping of simulation to experimental length scales, i.e., one bead roughly corresponds to 16 base pairs, the matching of time scales is more involved. If one matches loop extrusion times for SMC5/6, 1 x $10^6$ time steps in simulations roughly correspond to one second in experiments. For convenience, we used 1 x $10^6$ time steps as one second for all the simulation analysis.

For simulations we use the molecular dynamics package HOOMD-blue (*31*) on GPUs and CPUs. Equations of motion are integrated using a standard Langevin thermostat with dt = 0.01$\tau$ and $\gamma$= 0.1.

When calculating rates (loop, I, II), a 5-second interval (equivalent to 5 x $10^6$ time steps) was employed. For obtaining ratio-of-rates and $Rate_I$ vs $Rate_{II}$ analyses, any data points where either $Rate_I$ or $Rate_{II}$ fell

below 0.03 kbps (corresponding to three standard deviations of the noise in the traces) were excluded from further consideration.

**Modeling Loop Extrusion Symmetry from Experimentally Observed Translocation Rates**

We obtained translocation speeds for each Smc5/6 molecule by measuring their speed within three-second intervals, recording these along with the end-to-end distance of the DNA they translocated on (Fig. a-f). Analyzing DNA with different end-to-end distances (representing various relative extensions) provided translocation speeds at different relative extensions. Speed values were considered positive, as the initial direction for each molecule is random.

To model two physically linked translocating motors, we randomly selected two translocation speeds (for $Rate_I$ and $Rate_{II}$) from DNA molecules with the same relative extension. These rates were assigned negative signs, reflecting their action of reeling in DNA from outside to inside the loop, thus decreasing the sizes of segments I and II outside the loop. A 2D histogram was generated by extracting 10,000 such pairs of translocation speeds (Fig. 7g). However, slippage with positive segment rates was not modeled as translocation data lacks slippage information, resulting in population exclusively in Q3. This approach models loop extrusion rate variation without considering time/phase-dependent DNA tension changes.